


## Texture and strain analysis of tungsten films via Tilt-A-Whirl methodology

Mark A. Rodriguez <sup>a)</sup> Jamin Pillars, Nichole R. Valdez, James J. M. Griego, Matthew V. Gallegos, John A. Krukar, Andrew Polonsky, and Steven L. Wolfley  
Sandia National Laboratories, Albuquerque, NM 87185-1411, USA

(Received 13 May 2022; accepted 23 May 2022)

Tungsten (W) films have many applications in the semiconducting industry for sensor technology. Deposition conditions can significantly impact the resulting W films in terms of the phases present ( $\alpha$ -BCC or  $\beta$ -A12), microstructural grain orientation (texture), and residual strain. TILT-A-WHIRL methodology has been employed for the evaluation of a W film showing both texture and residual strain.  $\text{Sin}^2(\psi)$  analysis of the film was performed to quantify the strongly tensile in-plane strain (+0.476%) with an estimated in-plane tensile stress of  $\sim 1.9$  GPa. The 3D dataset was also evaluated qualitatively via 3D visualization. Visualization of 3D texture/strain data poses challenges due to peak broadening resulting from defocusing of the beam at high  $\psi$  tilt angles. To address this issue, principal component analysis (PCA) was employed to diagnose, model, and remove the broadening component from the diffraction data. Evaluation of the raw data and subsequent corrected data (after removal of defocusing effects) has been performed through projection of the data into a virtual 3D environment (via CAD2VR software) to qualitatively detect the impact of residual strain on the observed pole figure. © The Author(s), 2022. Published by Cambridge University Press on behalf of International Centre for Diffraction Data.  
[doi:10.1017/S0885715622000203]

Key words: strain analysis, tungsten films, Tilt-A-Whirl methodology

## I. INTRODUCTION

Transition edge sensor (TES) microcalorimeters are developing technology for single-photon detectors employed for detection of photon energies across the electromagnetic spectrum. TES sensors are held at temperatures just below the superconducting transition edge. In this state, even the smallest addition of energy (e.g. the absorption of a single photon) can cause very large changes in resistivity. Therefore, these devices are exceptionally sensitive and preferred for demanding diagnostic applications. TES sensors have found use for detecting near-infrared and optical energies (Lolli *et al.*, 2016) as well as X-ray energies (Jach *et al.*, 2007) and have found applications in astronomy and particle physics where low-background and weak signal detection are required (see Gottardi and Nagayashi, 2021). Cabrera *et al.* (1998) demonstrated the usefulness of W thin films as TES detectors for IR and visible photon energies. Tungsten sensors are very useful for a variety of energies because the transition temperature can be tuned for optimization of the superconducting transition edge. One means of tuning this transition temperature can be performed via adjustment of residual strain in the film. Hall (1965) demonstrated how residual strain can impact the superconducting transition temperature of tin films. More recently, Lita *et al.* (2005) and Abdelhameed *et al.* (2020) have shown how residual strain in W films can shift the TES temperature from 15 mK to as high as  $\sim 200$  mK depending on the strain condition of the deposited film. Control of the TES edge is

possible by controlling the deposition conditions; these include gas pressure, deposition temperature, and substrate material. These variables will have an impact on the texture, microstructure, in-plane residual strain (compressive or tensile), and possible phases of W that are formed. Because residual strain has such a significant impact on the outcome of the processed W film, we set out to measure the residual strain present in one of our deposited film samples and determine, both qualitatively and quantitatively, the measured strain present.  $\text{Sin}^2(\psi)$  measurements have been performed to extract this strain value quantitatively. However, there was also a desire to evaluate the strain and texture results visually. Our XRD data is three-dimensional (3D) and making use of newly developed tools for 3D visualization can aid in quickly and qualitatively evaluating the presence of compressive or tensile strain. This is accomplished by determining the warp direction of the 3D pole figures. We present our results, obtained using our “TILT-A-WHIRL” data-collection and data-reduction methodology (Rodriguez *et al.*, 2013) and document the challenging aspects of 3D pole figure visualization resulting from peak broadening at high  $\psi$  angles. This peak broadening is related to beam defocusing as the X-ray beam footprint enlarges across the film with sample tilt (increased  $\psi$  angle). We discuss data processing using principal component analysis (PCA) for removal of defocusing effects, thereby improving visualization of strain within the resulting 3D pole figures (plotted as  $\phi$ ,  $\psi$ , and  $2\theta$ ). A simple routine to separate the defocusing broadening from our 3D pole figure data is given that enables straightforward visualization of datasets. These new data analytics are applied to a textured W thin film with significant residual in-plane tensile strain.

<sup>a)</sup> Author to whom correspondence should be addressed. Electronic mail: marodri@sandia.gov

## II. EXPERIMENTAL

### A. W film deposition

Film deposition followed a similar process to that employed by Lita *et al.* (2005). The W film was deposited on a (100) oriented Si substrate using a Denton Discover 550 Sputter System with a high purity W target. Parameters for film deposition were 282 Watts sputter power and 7 mTorr Argon pressure. Film deposition time was 65 s and measured film thickness was 24 nm.

### B. XRD data collection

A Bruker D8 diffractometer was employed for XRD data collection using the TILT-A-WHIRL methodology (Rodriguez *et al.*, 2013). The D8 4-axis diffractometer was configured with Cu  $K\alpha$  radiation, a Vantec 2000 area-detector, and a texture cradle with an  $xyz$  translation stage. An incident-beam mirror optic was employed to remove Cu  $K\beta$  radiation and a 500  $\mu\text{m}$  pinhole collimator was used to create a small beam at the sample. A full 3D dataset was collected with dimensions of  $\phi$ ,  $\psi$ ,  $2\theta$  (spaghetti data), and processed via our in-house TILT-A-WHIRL software (Rodriguez *et al.*, 2013). Note  $\psi$  in this discussion is the same as the  $\chi$  angle. The term “spaghetti data” is used to relay the concept of a bundle of dry spaghetti. Such a bundle would form a cylinder where each separate strand would propagate along the axis of the cylinder. Each strand’s position in the bundle can be described using a polar grid ( $\psi$ ,  $\phi$ ) where the cross-section of the spaghetti bundle would plot out a pole figure and the cylinder’s axis would denote the  $2\theta$  axis of the 3D dataset. For more detail, see Rodriguez *et al.* (2013). To verify the proper alignment of the instrument, a  $\text{LaB}_6$  standard (NIST 660) was scanned to determine if there was any variation in peak location with  $\psi$  angle for an effectively zero-strain powder XRD standard. As in previous work, the  $\text{LaB}_6$  (311) peak at  $\sim 75.8^\circ$   $2\theta$  was employed (see Rodriguez *et al.*, 2020). The strain for the powder was determined to be  $-0.00019$  or  $-0.019(5)\%$  based on the slope of the  $\sin^2(\psi)$  plot (i.e.  $-0.019 \pm 0.005\%$ ). The strain error value of  $\pm 0.005\%$  was based on the fit and deviation of the straight line to the observed  $\Delta d/d_0$  values (Rodriguez *et al.*, 2020). The measured strain is very close to zero and confirms suitable alignment of the diffractometer for residual strain measurements. The  $-0.019\%$  value was taken as the instrument offset for strain and was used to correct any quantified strain values obtained on film samples via the  $\sin^2(\psi)$  method. However, due to this very low strain-offset value, we chose not to correct the full 3D datasets during the visualization process, as the change was negligible when compared to the peak shifts observed from residual strain in the film (i.e.  $<5\%$  of overall observed strain shift in the W film).

## III. RESULTS AND DISCUSSION

Figure 1 illustrates a series of XRD patterns as a function of  $\psi$  tilt for the W film. Although the TILT-A-WHIRL data-collection routine obtains data from 60  $\phi$  (spindle) rotations at any given  $\psi$  tilt angle, it can be very useful to obtain an initial assessment of the texture within a sample by merging the 60  $\phi$  patterns from each  $\psi$  tilt into a single scan. We refer to this series of  $\theta$ - $2\theta$  scans incremented by  $\psi$  as the “ $\phi$ -merged” scans. The  $\psi = 0$  scan (Figure 1, bottom pattern) represents the

normal (out-of-plane) condition for the sample and shows diffraction intensity from planes aligned with the film surface. As the  $\psi$  angle increases, one observes peaks diffracted from planes that display increasing tilt away from the surface, with the extreme case (not shown) at  $\psi = 90$  for planes fully perpendicular to the film surface. The maximum  $\psi$  tilt angle for our experiment was limited to  $78^\circ$ .

Note how significantly the W peaks shift with increasing  $\psi$  tilt. The W peaks also show substantial broadening (due to defocusing). Powder Diffraction File (PDF) entries (Gates-Rector and Blanton, 2109) for the various observed phases are shown in Figure 1, plotted below the XRD scans. The stick patterns show the  $\alpha$ -W phase (PDF entry 00-004-0806), and Si metal (PDF entry 00-027-1402). The ( $hkl$ ) labels for the various reflections of the  $\alpha$ -W phase are listed at the top of Figure 1. The results indicate that the W film is strictly body-centered-cubic (BCC)  $\alpha$ -W, with no detectable  $\beta$ -W phase (a.k.a A12) or other second phases. The film thickness was 24 nm, so the X-ray beam fully penetrates the film at all orientations of measurement. The observed Si peaks are from the underlying substrate and their intensity variation with  $\psi$  tilt is consistent with a (100)-oriented Si substrate. Validation of strictly  $\alpha$ -W for the film is important because the presence of  $\beta$ -W will impact the superconducting transition temperature ( $T_c$ ) and add an additional and unnecessary variable that can hamper tuning of the TES device.

Pole figures associated with the three  $\alpha$ -W peaks in the XRD dataset are presented in Figure 2. These pole figures are integrated across a range of  $2\theta$  values so as to represent the intensity distributions for these  $hkl$  indices. A rainbow color scale is used where high-intensity is red, and low-intensity is blue. Figure 2 (left) shows the  $\alpha$ -W (110) pole figure. This pole figure shows that the (110) planes have a preference to orient parallel to the substrate surface, thus creating the pole of intensity directly centered in the circular projection. Additionally, one observes a ring of increased counts at  $\sim 60^\circ$   $\psi$  tilt. The ring is continuous, indicative of an in-plane fiber texture for the deposited  $\alpha$ -W grains. The broadness of both the ring and central pole indicate that while the grains display a preferred orientation, the distribution (or mosaicity) of the polycrystalline  $\alpha$ -W grains is large ( $\sim 10$ – $15^\circ$ ). Figure 2 (middle) plots the observed (200) pole figure for the  $\alpha$ -W film. This figure shows a complementary result to that of the (110) pole figure. Specifically, the (200) pole figure lacks intensity in the center of the projection, and instead contains a ring of intensity in the  $40$ – $50^\circ$   $\psi$  range. This result is dictated by symmetry. With the (110) planes showing a preference for orienting parallel to the film surface, this constraint will demand that the preference for these same crystallites have their (200) planes tilted at  $\sim 45^\circ$   $\psi$  from the surface normal. Again, the presence of a ring of intensity in the (200) pole figure is consistent with an in-plane fiber texture. Figure 2 (right) shows the pole figure for the (211). This pole figure shows relatively constant intensity across the plot, until one reaches the edge where the intensity increases substantially. These data are raw data pole figures and were not corrected for defocusing, so the increase at the edge of the pole figure can be impacted by artifact intensity associated with defocusing. This artifact is more pronounced in the (211) pole figure because its intensity does not show as large of a scale change within the majority of the projection. This will be explained in more detail below.

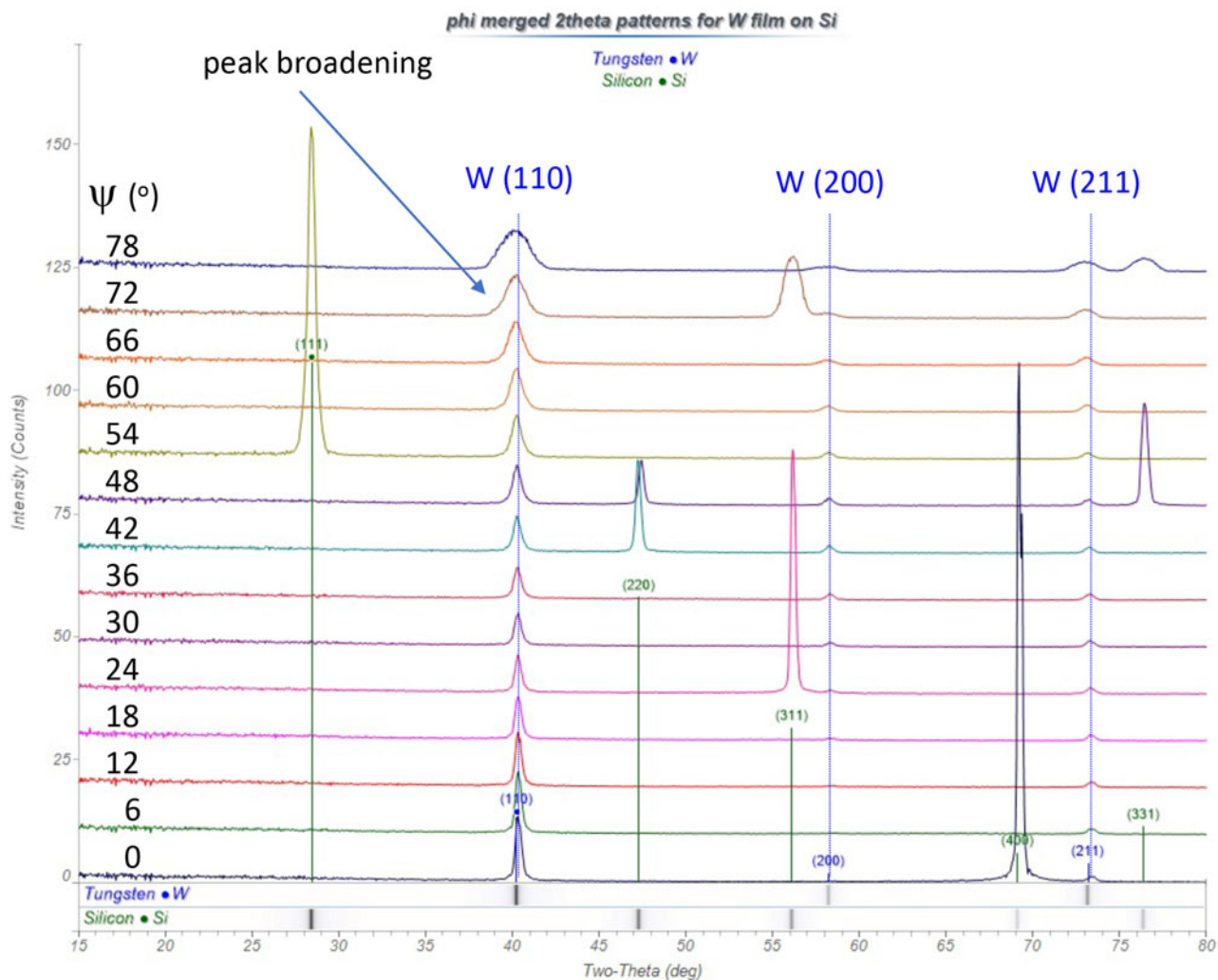


Figure 1.  $\phi$ -merged  $2\theta$  patterns showing peak shift of  $\alpha$ -W with increased  $\psi$  tilt angle. W peaks show broadening with increased  $\psi$  tilt due to beam defocusing. Si substrate peaks are also observed.

Figure 3 shows the plot of intensity as a function of  $\psi$  tilt. To generate this plot, the pole figure intensities at a given  $\psi$  angle were averaged over all  $\phi$  angles and then normalized to times-random by dividing by the average intensity value for a given pole figure. Figure 3 confirms peak maxima at  $\psi$

$= 0$  and  $\psi \sim 60^\circ$  for the (110) planes, and a peak maximum at  $\psi \sim 45^\circ$  for the (200) pole figure. Note, however, that the (211) intensity displays a nearly constant value with  $\psi$  angle (until the highest  $\psi$  values). This is a result of the (110) out-of-plane preferred orientation coupled with the in-plane

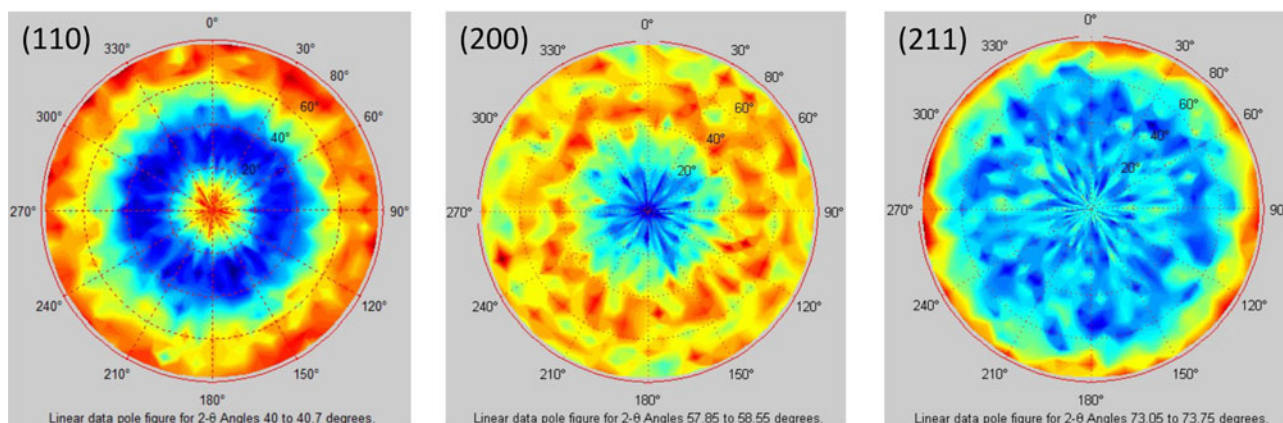


Figure 2. Raw data pole figures for the (110) – left, (200) – middle, and (211) – right, of the  $\alpha$ -W film as measured via the TILT-A-WHIRL method (high-intensity is red, and low-intensity is blue).



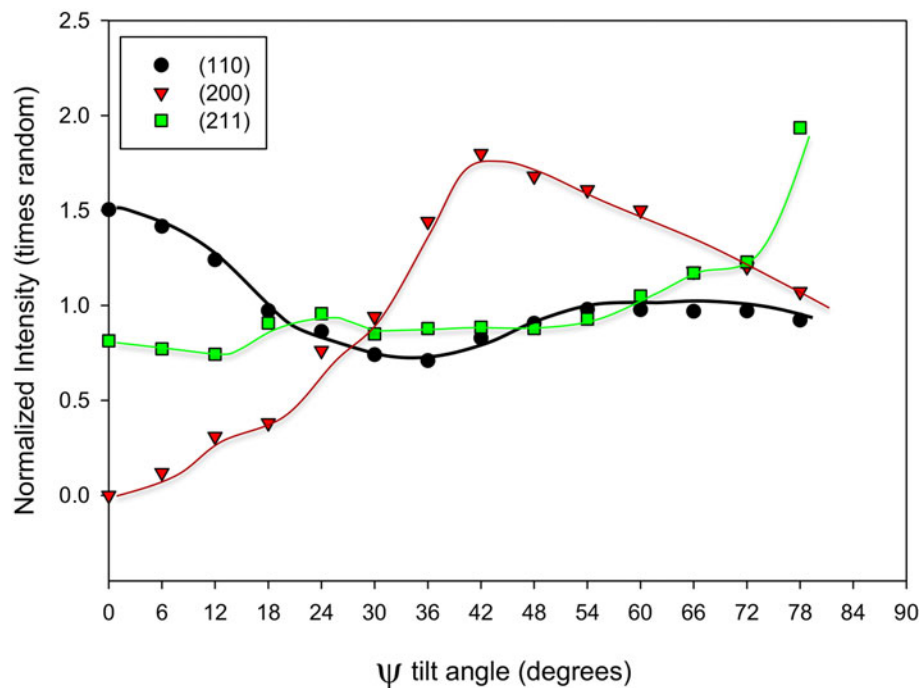


Figure 3. Times-random intensity distribution as a function of  $\psi$  angle for  $\alpha$ -W reflections.

fiber texture and is dictated by the interplanar angles between the (110) and (211) planes for this BCC structure. Symmetry dictates that for a (110) out-of-plane oriented film, the (211) planes can have many possible orientations resulting in intensity maxima at several  $\psi$  tilt angles. These maxima occur at  $\psi = 30^\circ, 54.7^\circ, 73.2^\circ,$  and  $90^\circ$  (Cullity, 1978). With the significant mosaicity of the film, these maxima will broaden out and overlap, resulting in the more uniform intensity with  $\psi$  tilt angle.

There are indications of significant residual strain in this film. It is clear from Figure 1 that the  $\alpha$ -W peaks shift with  $\psi$  tilt. Another means of determining the presence of strain is by evaluating the pole figure data. If one chooses to plot the pole figure using data from separate sides of the diffraction peak, one can observe differences in the resulting pole figure projections due to the strain. Figure 4 shows this method, and the resulting pole figures observed. The  $\phi$ -merged  $2\theta$  scans shown in Figure 4 are a zoomed-in region of Figure 1 to highlight the  $\alpha$ -W (110) peak. In Figure 4, we clearly see the shift in the  $\phi$ -merged  $2\theta$  scans to lower  $2\theta$  angle with increased  $\psi$  tilt. If one integrates the pole figure intensity over a limited range of  $2\theta$  on either side of the  $\alpha$ -W (110) peak maxima at  $\psi = 0$ , we observe that these regions of integrated intensity generate significantly different pole figures depending on if the selected  $2\theta$  range is on the high or low-angle side of the (110) reflection. The reasoning behind generating these two pole figures is to show how different the pole figures look as a result of the in-plane strain. The pole figure on the high-angle side shows loss of intensity in the outer portion of the pole figure, while the pole at the low-angle side of the peak shows a much greater ring of intensity at  $\psi > 50^\circ$ . This non-uniform intensity distribution is due to the intensity shift in  $2\theta$  caused by residual strain and is indicative of a significant tensile strain present in the film. Such diagnosis can serve to quickly identify the presence of residual strain in a film sample.

#### A. Detection of residual strain in W film

The  $\alpha$ -W (211) peak was selected for use in the residual strain determination of the film because it (1) was relatively isolated and unobstructed by any other peaks in the patterns, (2) showed sufficient intensity for peak fitting with consistent intensity over a large range of  $\psi$  tilts, and (3) was at a reasonably high angle in  $2\theta$  to improve sensitivity to small changes in  $d$ -spacing that are required for the strain determination method. Figure 5 shows the resulting  $\Delta d/d_o$  vs.  $\sin^2(\psi)$  for the  $\alpha$ -W film. For this analysis, it is assumed that the film has a bi-axial stain behavior (common for thin films). Therefore, the out-of-plane  $d$ -spacing value for the  $\alpha$ -W (211) peak has been assigned as the  $d_o$  value. We employed the  $\phi$ -merged data for the  $\sin^2(\psi)$  analysis. The use of the  $\phi$ -merged scans is reasonable as the film displays a fiber texture and this method would improve the signal/noise for the  $2\theta$  scans as a function of  $\psi$ . Figure 5 shows the  $\sin^2(\psi)$  plot for the  $\alpha$ -W (211) reflection. The plot displays a strong positive slope, indicative of a large in-plane tensile strain. The magnitude of the strain was measured as  $+0.457(3)\%$ , and after correction for the  $\text{LaB}_6$  offset of  $0.019\%$  was determined to be  $+0.476(3)\%$  tensile in-plane strain. Taking the Young's modulus for W as 405 GPa (as per Grünwald *et al.*, 2015), the resulting estimated in-plane stress was calculated to be 1.93 GPa. This value, while very large, is comparable with Lita *et al.* (2005) who found tensile in-plane stresses in their W films on the order of 1.3 GPa.

#### B. Data preparation for 3D visualization

It is possible to port 3D data into virtual reality (VR) for viewing in 3D; however, the defocusing effects cause the  $\alpha$ -W peaks at high  $\psi$  tilt angles to become very broad. One can see the effects of this broadening in the raw data for the  $\alpha$ -W (211) peak. For example, Figure 6 shows data (as waterfall plots) for

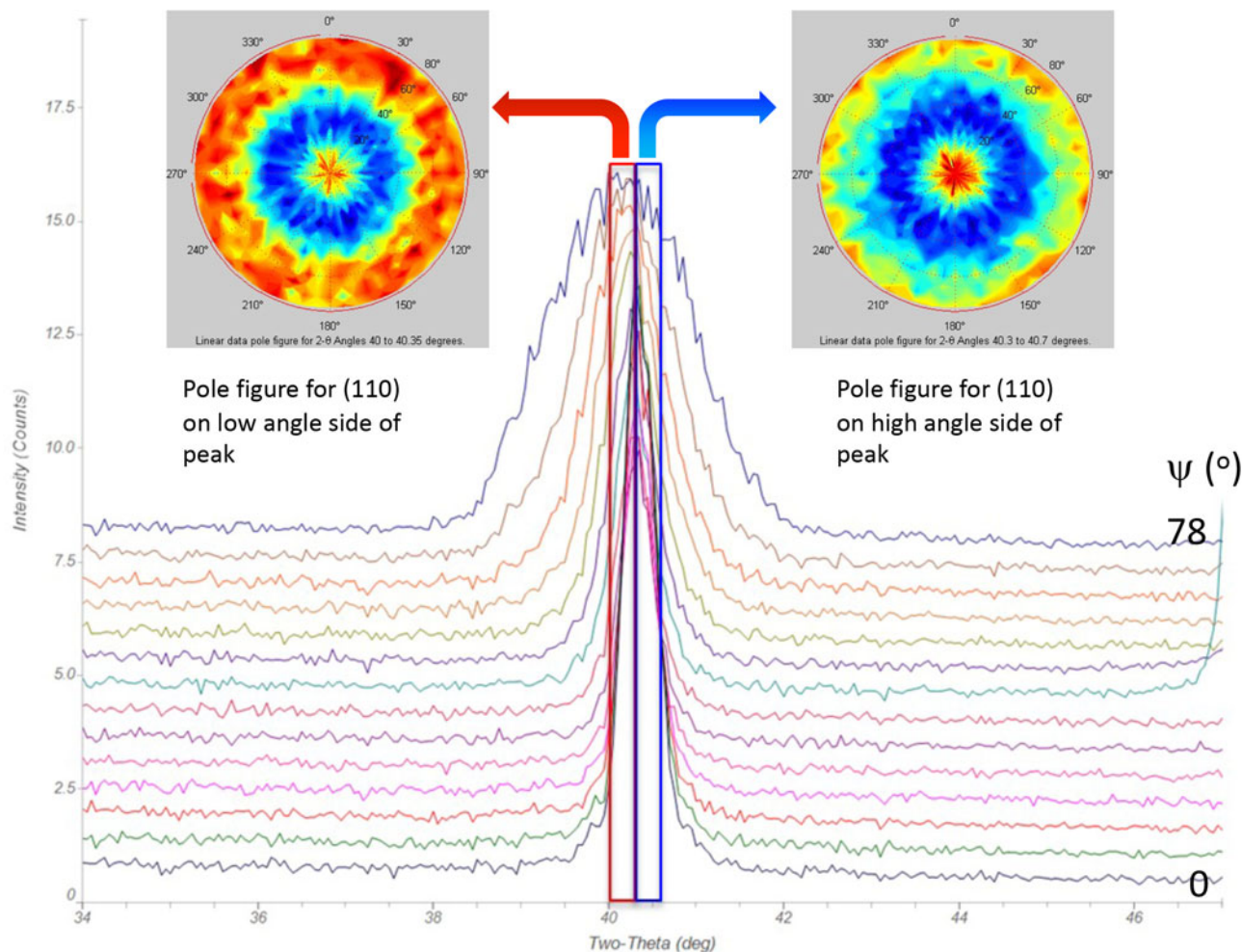


Figure 4.  $\alpha$ -W (110) pole figures generated from intensity on either side of the (110) peak.

all 840 scans taken at different  $\psi$  and  $\phi$  orientations. Full TILT-A-WHIRL datasets require collection times of  $\sim 20$  h. However, a limited range like that shown in Figure 6 would require  $< 1$  h with the use of an area detector. In Figure 6 (top), we plot the raw data for all the measured (211) peaks. One can see that at the highest  $\psi$  values, plotted here as increasing scan number on the  $x$ -axis, there is substantial

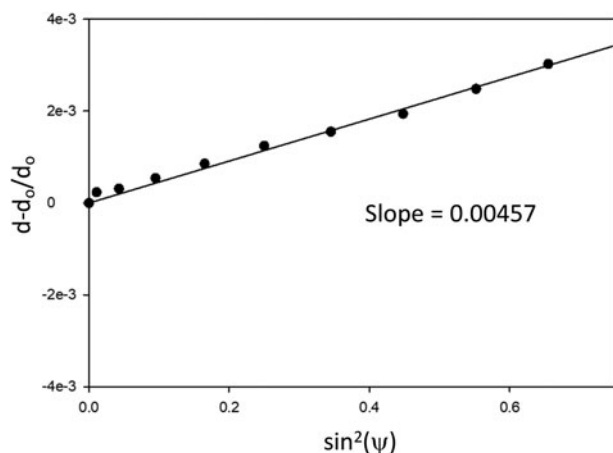


Figure 5.  $\sin^2(\psi)$  plot of  $\alpha$ -W (211) confirming strong in-plane tensile strain in the film.

broadening (e.g. scan numbers greater than 600). This issue can make visualization somewhat difficult for residual strain as we are looking to visually detect a bowing of the intensity distribution with  $\psi$  tilt; the broadening from beam defocusing can cause the pole figure to flare out in both directions of  $2\theta$ , thereby making a 3D-plotted pole figure wide at the pole figure edges (i.e. high  $\psi$  values). This artifact makes viewing of the pole figure distortion in the  $2\theta$  dimension (i.e. concave or convex warping) more difficult, as will be demonstrated below. In order to overcome these issues, we performed PCA to extract the defocusing effects from the 3D data for improved viewing in 3D. PCA is a useful technique for reducing large datasets into more useful “components” for further analysis. The components, isolated from each other via statistical algorithms, serve to parse data and thereby enable isolation and extraction of relevant signal from that of artifact or noise (e.g. see Rodriguez *et al.*, 2007).

The PCA analysis was not as straightforward as initially envisioned. Initial attempts to perform PCA on the raw data proved difficult as the broadening and strain aspects of the dataset would not factor independently. In order to aid in the isolation and extraction of the defocusing function from the data, we first pre-processed the spaghetti data over a limited range of the 3D dataset, namely a range of  $71.5^\circ$ – $75.0^\circ$   $2\theta$  (Figure 6, top). The first step in the pre-processing of the data was to smooth the spaghetti data. Figure 6 (middle)

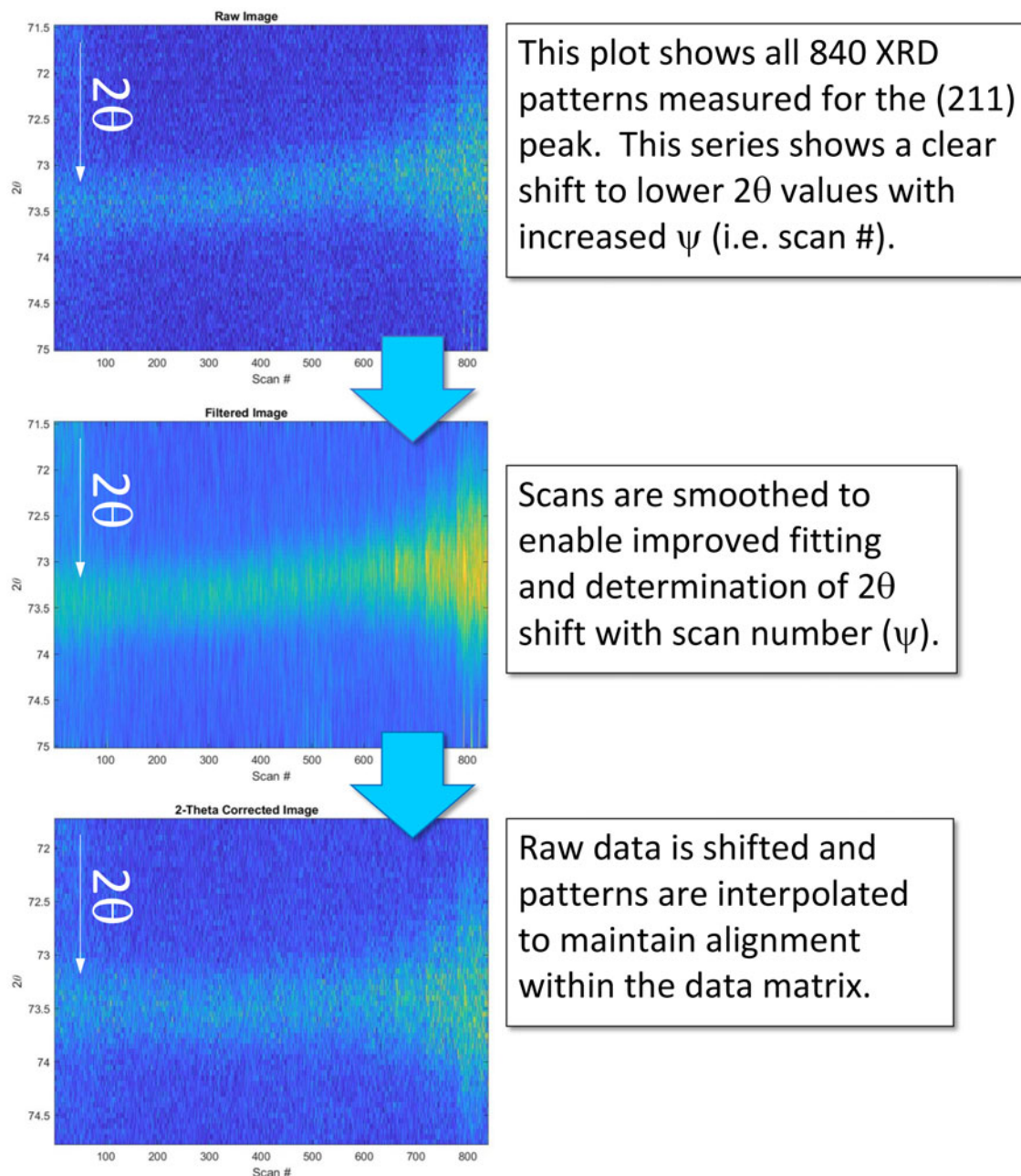


Figure 6. Process of preparing spaghetti data of  $\alpha$ -W (211) for defocus correction. Top image shows raw data for (211) peak; middle image shows smoothed data; and bottom image shows modeling and shifting of scans to remove strain. Yellow is high intensity, blue is low intensity.

shows the data after smoothing. Next, this smoothed data was profile-fit to determine the center of maximum intensity of each of the 840 (211)  $2\theta$  scans. The  $2\theta$  positions for each scan were stored for later use as they represented the shift in  $2\theta$  due to residual strain for the film relative to the  $\psi = 0$  (normal) scan. Next, the raw spaghetti data scans for the (211) reflection were aligned so that the  $2\theta$  values coincided with the  $2\theta$  value of the  $\psi = 0$  scan. Note,  $d_o$  was assumed to correspond to the  $\psi = 0$  (normal) scan. Figure 6 (bottom) shows the waterfall plot after this shift was completed. The shift was performed on the raw data; the smoothed data was only employed to determine the  $2\theta$  shift value. Note that the patterns in Figure 6 (bottom) required interpolation to maintain alignment within the data matrix. At this point, the shift in peak position due to strain was effectively removed (but stored for use later) and the data were ported to PCA analysis.

By pre-processing the data to nullify the peak shift due to strain, the PCA analysis was easily performed to determine the broadening artifact in the data. Figure 7 shows the results of the PCA analysis. The Eigen analysis (not shown) indicated a straightforward Rank 2 behavior for the dataset. For more detail regarding Eigen analysis, see Rodriguez *et al.* (2007). Factors 1 and 2 are shown in Figure 7 and illustrate both the factor weights (left) and scores (right). The Factor 1 weighting (as plotted in Figure 7, left) appears to represent the average peak profile shape for the (211) reflection for all scans. The scores for Factor 1 show its variation in magnitude with scan number, which is likely associated with the texture in the film. The trend in the intensity (score magnitude) for Factor 1 (Figure 7, right) is similar to the plot of the times-random intensity for the  $\alpha$ -W (211) given in Figure 3. The weightings for Factor 2 (see Figure 7, left) show an



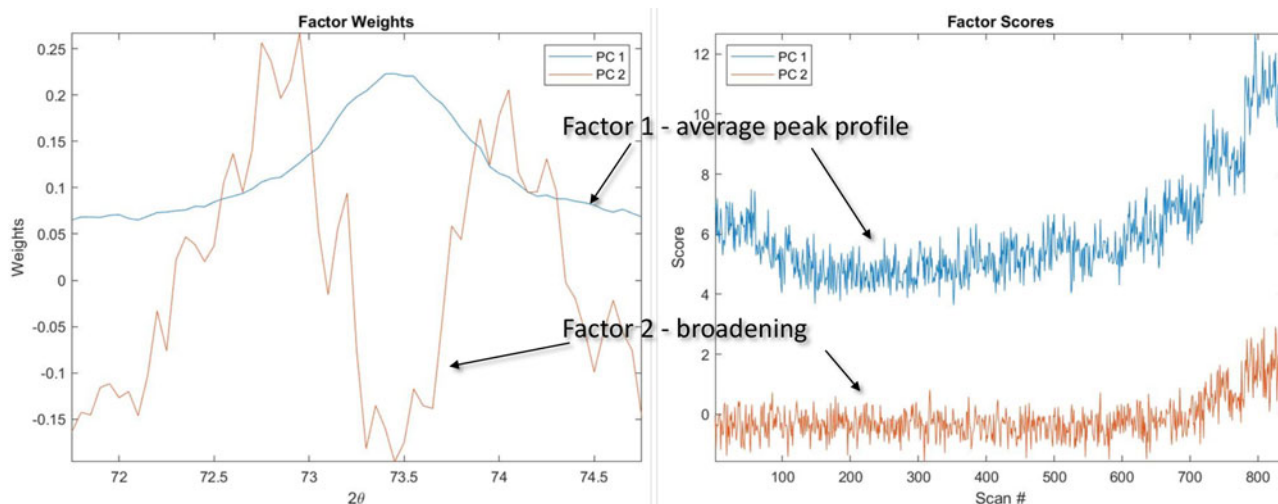


Figure 7. PCA analysis of pre-processed spaghetti data for  $\alpha$ -W (211) peak. Left: extracted components (weights) from the full dataset showing Factor 1 as the average peak profile and Factor 2 as the broadening function due to defocusing. Right: extracted scores associated with Factors 1 and 2 illustrating how these functions behave with increasing  $\psi$  (scan #).

oscillatory function, with peak maxima occurring on either side of the average peak position observed from Factor 1. This oscillatory function is consistent with that of a broadening function for a peak profile. The scores for Factor 2 (Figure 7, right) show that this factor only seems to play a role at the highest scan numbers, namely scans in the  $\psi = 66^\circ, 72^\circ,$  and  $78^\circ$ . Thus, having identified the broadening factor with its weights and scores (i.e. Factor 2), this portion of the data can be isolated and removed from the 3D dataset and thereby exclude the broadening effects from the data. This was easily performed by regenerating the diffraction patterns from Factor 1 via multiplication of the weights and scores matrices. The benefit of PCA is that it also identifies other factors that may be considered noise in the data. Higher order Factors in the Eigen analysis all proved to be related to noise in the dataset. By excluding all but the data associated with Factor 1, the net result serves to isolate the desired pole figure data from that of the undesired broadening effects *and* any noise assigned to higher factors in the PCA analysis. Hence, the PCA analysis serves an additional purpose of removing noise from the data while successfully factoring out the defocusing effects.

After isolating on Factor 1 for further analysis, the data were corrected back to their original angular positions based on the stored values of shift for each scan. Figure 8 shows the resulting process where the data extracted from PCA as exclusively Factor 1 (Figure 8, top) is reconstructed as spaghetti data, and then subsequently shifted back to each scan's original  $2\theta$  position (Figure 8, bottom) as determined prior to PCA (see Figure 6, middle). This 3D dataset is now ready for visualization as a 3D pole figure where the defocus error has been modeled and removed.

### C. 3D strain visualization via 3D pole figure projection into virtual reality

Data from Figure 8 (bottom) were reconstructed as a 3D pole figure over the limited range of  $2\theta$  and ported as 2D ( $\phi, \psi$ ) slices at a fixed  $2\theta$  value. The intensity was scaled to a 256-color scaling of intensity for the  $\alpha$ -W (211) pole figure.

This format enabled the generation of a Tiff-stack of images to port into VR using Sandia's in-house CAD2VR software (<https://cad2vr.sandia.gov/>). The CAD2VR software allows for projection of 3D data from many formats including raw Tiff images or CAD-formatted drawings and then these datasets can be viewed and manipulated in VR. We also performed the same data extraction and Tiff-stack dataset generation using the original raw data of the  $\alpha$ -W (211) pole figure for comparison.

Figure 9 (left) shows the original raw data for the  $\alpha$ -W (211) pole figure as projected into VR as a 3D dataset. First note that the background looks much like a warehouse. This is intentional and serves to give depth and perspective to objects viewed in the VR environment. Also note that this pole figure has been *bisected in half*, revealing the interior intensity distribution through the cross-section. This was done on purpose to better view the variation of intensity with  $\psi$  tilt as one pans across the  $2\theta$  thickness of the pole figure, which would be the characteristic of the presence of strain. Note, in the pole figure  $2\theta$  is orthogonal to  $\psi$  and  $\phi$ . The labels on the 3D view indicate the different angles employed for plotting the data, with  $\phi$  the rotation axis (in this case  $0-180^\circ$ )  $\psi$  starting in the middle of the cross-section and spanning to the end of the pole figure ( $0-78^\circ$ ) and  $2\theta$  plotted through the thickness of the pole figure data itself ( $71.5^\circ-75.0^\circ 2\theta$ ). When comparing the data from the raw (left) and defocus-corrected (right) in Figure 9, it is clear that the intensity internal to the  $2\theta$  thickness is better-resolved and the noise level is reduced after PCA processing. This has much to do with the smoothing aspect of the PCA factor analysis. However, it is still difficult to determine from this view whether the intensity distribution shows a warp to lower or higher  $2\theta$  with increased  $\psi$  angle as partially illustrated in Figure 4. Fortunately, there are essentially unlimited orientations possible when using the CAD2VR application, and the data can be positioned ideally for viewing in any orientation with intuitive and easy to use game-like controls. This makes speed of analysis much faster and generates immediate feedback for those evaluating the data.

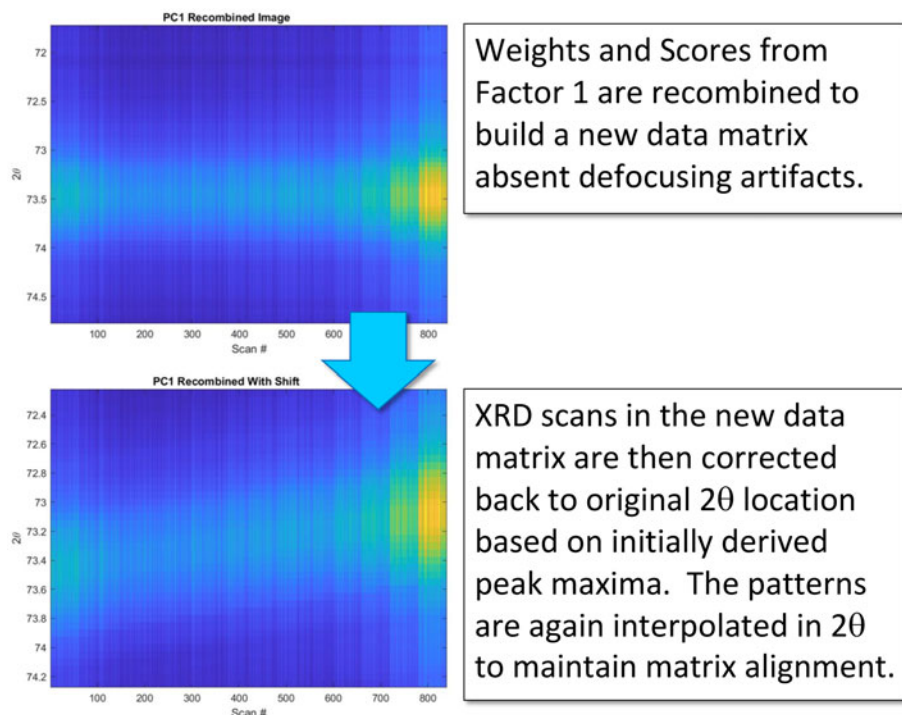


Figure 8. Waterfall plots for post-PCA spaghetti data. (Top) Reconstruction of spaghetti data for Factor 1 exclusively. (Bottom) Factor 1 after re-assigning peak locations based on initially determine strain shift in  $2\theta$ .

For a more informed view of the strain in the cross-sectioned pole figure, the data were reoriented in VR to show a view nearer to straight-on the sectioned pole figure.

Figure 10 shows this view of the cross-sectioned pole figures where our perspective is nearly perpendicular to the  $2\theta$  axis. This alternative vantage point allows for a clear perspective

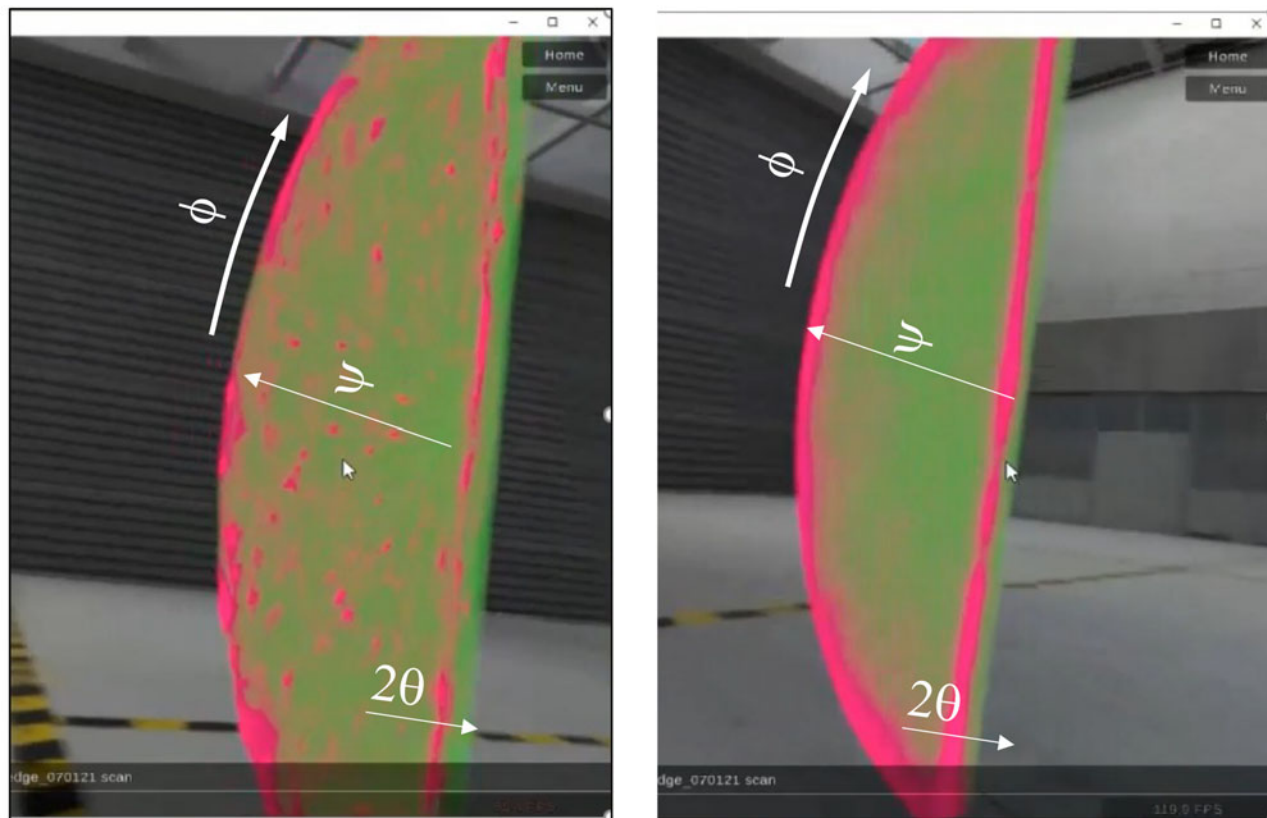


Figure 9. Cross-sectioned pole figures for  $\alpha$ -W (211) low counts (green) and high counts (magenta). Left: raw data showing original pole figure result prior to PCA correction. Right: pole figure cross-section of Factor 1 dataset with reduced noise and clearer features.



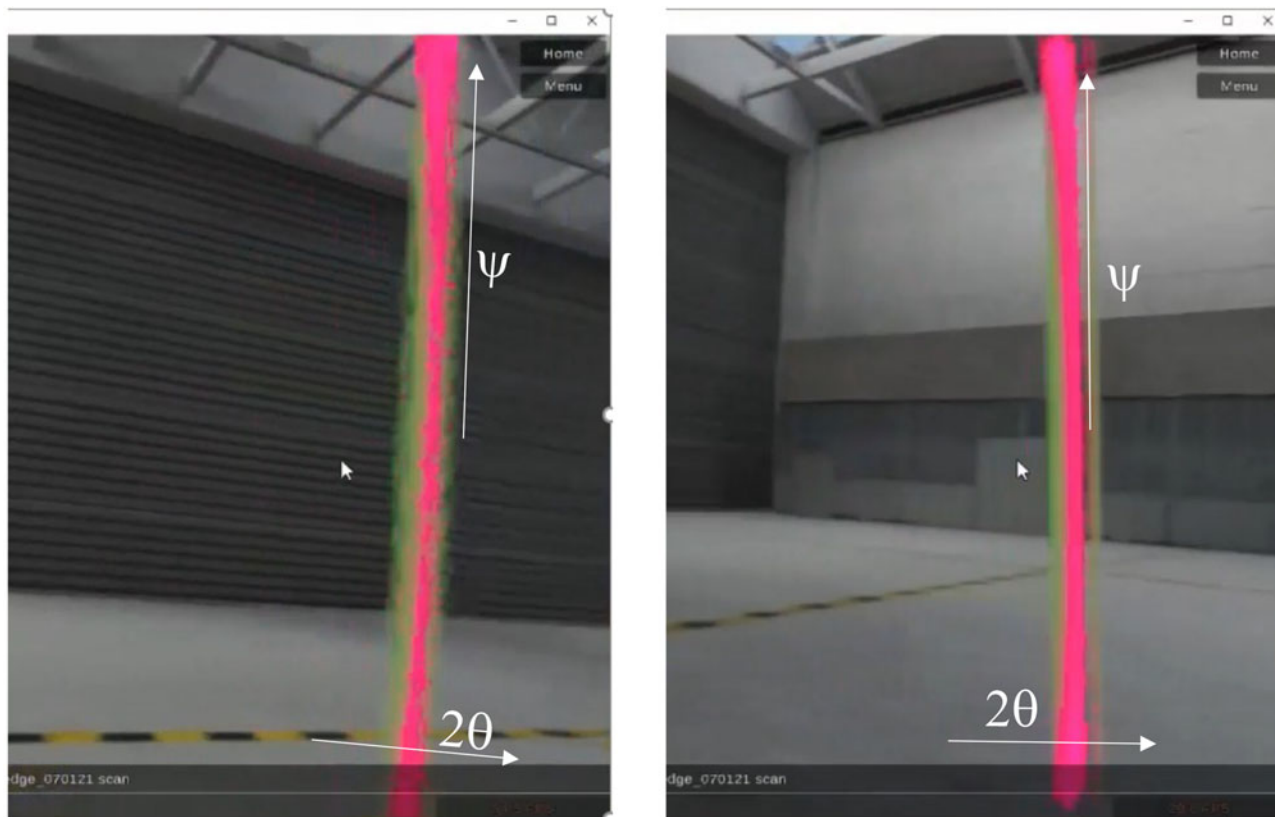


Figure 10. Reoriented view of cross-sectioned pole figures for  $\alpha$ -W (211); low counts (green) and high counts (magenta). Left: raw data showing possible warp in intensity along  $\psi$  direction. Right: pole figure cross-section of exclusively Factor 1 dataset with reduced noise and clearer detection of concave warp toward lower  $2\theta$  indicating presence of in-plane tensile strain.

on the shifting of intensity from center to edge ( $\psi$  angle). Figure 10 (left) shows the original raw data result for this view. It is possible to see a trend in the image to lower  $2\theta$  from the center to the edge of the pole figure, and the intensity appears to warp and bow toward lower  $2\theta$  at the higher  $\psi$  values. This is as expected. However, the intensity does broaden substantially at the perimeter of the pole figure due to the defocus errors. In contrast, Figure 10 (right) shows the 3D pole figure data after processing via PCA to remove broadening and noise. This image shows a much cleaner intensity distribution when the  $\alpha$ -W (211) pole figure is bisected. The data in Figure 10 (right) clearly show a concave warp in the intensity distribution as one moves to higher  $\psi$  tilt angles. In addition, while the intensity at the edge of the perimeter of the pole figure is still high, the broadening of the intensity has appeared to be reduced due to the extraction of the broadening component caused by defocusing. Hence, Figure 10 illustrates the usefulness of the data correction process via PCA for visualizing subtle but detectable features in XRD data. Note that Figure 10 (right) is intensity data exclusive to Factor 1. While the extremes in  $\psi$  position for Figure 10 (right) still look broadened, this appearance is more associated with the magnitude of intensity at these high  $\psi$  angles. The benefit of viewing in VR is that the environment allows the user full access to 3D data as well as tools for manipulation so that analysis can be performed on-the-fly. In this case, it was immediately obvious that the  $\alpha$ -W film exhibited a significant in-plane tensile strain.

The CAD2VR software has enabled coincident viewing of rendered 3D data. This software platform allows multiple users to simultaneously view 3D datasets either in VR (via a

headset) or via their computer screen with keyboard and mouse controls. This feature allows for real-time interactions where detailed discussions are possible via an audio link. In fact, data in Figures 9 and 10 were generated during just such an online meeting where two of the authors (MVG and MAR) simultaneously viewed the 3D data and extracted the desired output after a few iterations and online interactions. This ability for a multi-user environment enables synergy and enhances productivity by more seamlessly communicating 3D data to many customers via a single meeting. The ability for detailed discussion and enhanced interrogation of data can help a team to obtain answers faster and with higher confidence. This new VR work environment serves as a much-needed tool for communication and evaluation of 3D data for customers across the hall or colleagues across the country via the internet.

#### IV. SUMMARY

We have demonstrated a means of measuring residual strain in W films via our TILT-A-WHIRL methodology. This XRD technique enables detailed  $\sin^2(\psi)$  analysis for quantification of residual strain in thin films. In this work, a tensile in-plane strain of 0.476% was observed for a sputter-deposited  $\alpha$ -W film deposited on a Si wafer, corresponding to an estimated 1.93 GPa in-plane stress for the film. The  $\alpha$ -W film showed an out-of-plane (110) preferred orientation with an in-plane fiber texture. The use of PCA for extraction of the defocusing effects present in the data allowed for improved 3D visualization and facilitated the detection of warping of intensity within the pole figure as a result of  $2\theta$  peak shift of

the (211) reflection with  $\psi$  tilt. The use of CAD2VR served as a useful platform for 3D XRD data visualization for texture and strain.

## ACKNOWLEDGEMENTS

This work is supported by the Laboratory Directed Research and Development program at Sandia National Laboratories, a multimission laboratory managed and operated by the National Technology and Engineering Solutions of Sandia, LLC., a wholly owned subsidiary of Honeywell International, Inc., for the U.S. Department of Energy's National Nuclear Security Administration under contract DE-NA-0003525.

## CONFLICTS OF INTEREST

The authors have no conflicts of interest to declare.

Abdelhameed, A. H., Angloher, G., Bauer, P., Bento, A., Bertoldo, E., Canonica, L., Fuchs, D., Hauff, D., Ferreira Iachellini, N., Mancuso, M., Petricca, F., Probst, F., Riesch, J. and Rothe, J. (2020). "Deposition of tungsten thin films by magnetron sputtering for large-scale production of tungsten-based transition-edge sensors," *J. Low Temp. Phys.* **199**, 401–407.

Cabrera, B., Clarke, R. M., Colling, P., Miller, A. J., Nam, S. and Romani, R. W. (1998). "Detection of single infrared, optical, and ultraviolet photons using superconducting transition edge sensors," *Appl. Phys. Lett* **73**, 735–737.

Cullity, B. D. (1978). *Elements of X-Ray Diffraction* (Addison-Wesley, Reading, MA), 2nd ed., p. 75.

Gates-Rector, S., and Blanton, T. (2019). "The Powder Diffraction File: a quality materials characterization database," *Powder Diffr.* **34**, 352–360.

Gottardi, L., and Nagayashi, K. (2021). "A review of X-ray microcalorimeters based on superconducting transition edge sensors for astrophysics and particle physics," *Appl. Sci.* **11**(3793), 1–44.

Grünwald, E., Nuster, R., Treml, R., Kiener, D., Paltauf, G., and Brunner, R. (2015). "Young's modulus and Poisson's ratio characterization of tungsten thin films via laser ultrasound," *Mater. Today: Proc.* **2**, 4289–4294.

Hall, P. M. (1965). "Effect of stress on the superconducting transition temperature of thin films of tin," *J. Appl. Phys.* **36**, 2471–2475.

Jach, T., Ritchie, N., Ullom, J., and Beall, J. A. (2007). "Quantitative analysis with the transition edge sensor microcalorimeter X-ray detector," *Powder Diffr.* **22**, 138–141.

Lita, A. E., Rosenberg, D., Nam, S., Miller, A. J., Blazar, D., Kaatz, L. M., and Schwall, R. E. (2005). "Tuning of tungsten thin film superconducting transition temperature for fabrication of photon number resolving detectors," *IEEE Trans. Appl. Supercond.* **15**, 3528–3531.

Lolli, L., Taralli, E., Portesi, C., Rajteri, M., and Monticone, E. (2016). "Aluminum–titanium bilayer for near-infrared transition edge sensors," *Sensors* **16**(953), 1–7.

Rodríguez, M. A., Keenan, M. R., and Nagasubramanian, G. S. (2007). "In situ X-ray diffraction analysis of  $(\text{CF}_x)_n$  batteries: signal extraction by multivariate analysis," *J. Appl. Crystallogr.* **40**, 1097–1104.

Rodríguez, M. A., Pearl, M. R., Van Benthem, M. H., Griego, J. J. M., and Pillars, J. R. (2013). "Tilt-A-Whirl: a texture analysis package for 3D rendering of pole figures using matlab," *Powder Diffr.* **28**, 81–89.

Rodríguez, M. A., Harrison, K. L., Goriparti, S., Griego, J. J. M., Boyce, B. L., and Perdue, B. R. (2020). "Use of a Be-dome holder for texture and strain characterization of Li metal thin films via  $\sin^2(\psi)$  methodology," *Powder Diffr.* **35**, 89–97.